New Journal of Physics
The open access journal at the forefront of physics

Deutsche Physikalische Gesellschaft DPG
IOP Institute of Physics

Published in partnership with: Deutsche Physikalische Gesellschaft and the Institute of Physics

OPEN ACCESS

RECEIVED
1 June 2015

REVISED
7 September 2015

ACCEPTED FOR PUBLICATION
21 September 2015

PUBLISHED
16 October 2015

PAPER

Proton acceleration enhanced by a plasma jet in expanding foils undergoing relativistic transparency

H W Powell[1], M King[1], R J Gray[1], D A MacLellan[1], B Gonzalez-Izquierdo[1], L C Stockhausen[2], G Hicks[3], N P Dover[3], D R Rusby[1,4], D C Carroll[4], H Padda[1], R Torres[2], S Kar[5], R J Clarke[4], I O Musgrave[4], Z Najmudin[3], M Borghesi[5], D Neely[4] and P McKenna[1]

[1] SUPA Department of Physics, University of Strathclyde, Glasgow G4 0NG, UK
[2] Centro de Láseres Pulsados (CLPU), M5 Parque Científico, E-37185 Salamanca, Spain
[3] The John Adams Institute for Accelerator Science, Blackett Laboratory, Imperial College London, London SW7 2BZ, UK
[4] Central Laser Facility, STFC Rutherford Appleton Laboratory, Oxfordshire OX11 0QX, UK
[5] Centre for Plasma Physics, Queens University Belfast, Belfast BT7 1NN, UK

E-mail: paul.mckenna@strath.ac.uk

Keywords: laser–plasma interactions, relativistic transparency, ion acceleration, plasma jet

Supplementary material for this article is available online

Abstract

Ion acceleration driven by the interaction of an ultraintense (2×10^{20} W cm^{-2}) laser pulse with an ultrathin ($\leqslant$40 nm) foil target is experimentally and numerically investigated. Protons accelerated by sheath fields and via laser radiation pressure are angularly separated and identified based on their directionality and signature features (e.g. transverse instabilities) in the measured spatial-intensity distribution. A low divergence, high energy proton component is also detected when the heated target electrons expand and the target becomes relativistically transparent during the interaction. 2D and 3D particle-in-cell simulations indicate that under these conditions a plasma jet is formed at the target rear, supported by a self-generated azimuthal magnetic field, which extends into the expanded layer of sheath-accelerated protons. Electrons trapped within this jet are directly accelerated to super-thermal energies by the portion of the laser pulse transmitted through the target. The resulting streaming of the electrons into the ion layers enhances the energy of protons in the vicinity of the jet. Through the addition of a controlled prepulse, the maximum energy of these protons is demonstrated experimentally and numerically to be sensitive to the picosecond rising edge profile of the laser pulse.

1. Introduction

The strong electric fields excited in dense plasma by intense laser pulses enable the acceleration of ions to multi-MeV energies over short (micron-scale) distances. The resulting ion beams can potentially be used for wide-ranging applications, including cancer therapy, radiography and fast ignition-fusion [1]. The need to enhance the ion energies and to control the beam properties for many applications motivates efforts to develop new acceleration mechanisms and investigate the underpinning physics.

In the case of sub-micron-thick target foils several distinctly different acceleration mechanisms can occur. Target normal sheath acceleration (TNSA) [2] results from an electrostatic field formed by fast electrons transported through the target that are thermalised at the rear side and undergo expansion leading to a space-charge separation of ions. This produces a divergent ion beam with a thermal spectrum. Radiation pressure acceleration (RPA) [3] is a promising alternative scheme in which the target front surface is driven forward by laser light pressure, and is predicted to result in a narrow energy spectrum and low divergence ion beam, with more favourable intensity scaling [4, 5]. In nanometer-thick foils RPA has been shown to be sensitive to transverse, Rayleigh–Taylor-like instabilities which give rise to bubble-like features in the proton beam [6]. The effectiveness of RPA is diminished if the target becomes transparent to the laser light during the interaction. This occurs if the target electron population is compressed such that the thickness of the electron layer is less than the skin depth or expands such that the peak electron density, n_e, decreases below the critical density,

$n_c = m_e \epsilon_0 \omega_L^2 / e^2$ (the density at which the plasma frequency is equal to the laser frequency), where m_e is the electron rest mass, ϵ_0 is the vacuum permittivity, ω_L is the angular laser frequency and e is the electron charge [7]. With linearly-polarized laser pulses at the peak intensities achievable presently, transparency is usually induced via a combination of decreasing n_e due to electron expansion and an increase of the relativistically-corrected critical density (γn_c, where γ is the electron Lorentz factor) on the rising edge of the laser pulse intensity profile [8]—hereinafter referred to as relativistically induced transparency (RIT) [7].

RIT occurring at the front side of a target with a density gradient matched to the rising laser pulse intensity profile can lead to the acceleration of light ions by reflection from a moving electrostatic potential generated by an increase in the local electron density — a process termed RITA [9]. In the case for which the full target thickness becomes transparent due to RIT, the resulting volumetric heating of electrons by the transmitted portion of the laser pulse enhances the maximum energy of TNSA-ions, in a scheme called break-out afterburner (BOA) [10, 11]. The relativistic-Buneman electron-ion two stream instability has been invoked to account for energy transfer between the co-directional electrons and ions in the BOA scheme [12]. The highest BOA ion energies are reported to be observed at an angle to the laser propagation axis [11]. In thin foils which undergo significant expansion, such that the laser pulse propagates through an extended near-critical density plasma slab, magnetic vortex acceleration of ions, in the direction of decreasing plasma density, can also occur [13, 14]. Although recently Wagner *et al* [15] have shown that it is possible to angularly separate beams produced by different acceleration mechanisms, in typical experiments involving near-normal laser incidence, fast ions produced by individual acceleration mechanisms are not unambiguously distinguished in integrated spectral and spatial measurements. This impedes their investigation and optimization.

In this article, ultraintense laser-driven proton acceleration from ultrathin target foils undergoing expansion and RIT is experimentally and numerically investigated. The angular separation and detection of signature components of TNSA and RPA indicate that both of these mechanisms occur. The physics underpinning energy enhancement in a high-energy, directional part of the proton beam is investigated. It is found, for the first time, that this is driven by the formation of a plasma jet, supported by a self-generated quasi-static magnetic field, at the target rear side. Direct laser acceleration of electrons which are trapped within the jet by the magnetic field significantly enhance their energy. These electrons stream through the sheath-accelerated proton layer, driving an electrostatic field which transfers energy to protons within a narrow angular range in the vicinity of the jet. Through the introduction of a controlled prepulse, it is shown that the final maximum proton energy is increased by a factor which is highly sensitive to the rising edge intensity profile of the laser pulse on the picosecond timescale.

2. Experiment results

The 1.054 μm wavelength Vulcan laser at the Rutherford Appleton Laboratory was used. It was configured to deliver either a single pulse with duration equal to (1.0 ± 0.2) ps (full width at half maximum, FWHM) or a main pulse with a (1.0 ± 0.2) ps lower intensity prepulse, with peaks separated by (1.5 ± 0.1) ps. The latter mode effectively corresponds to a change in the intensity profile of the rising edge of the main pulse. This was achieved by introducing a prepulse after the first stage of pre-amplification and before the pulse stretcher, using a polarizer and polarizing beam splitter to control the energy. The total laser pulse energy (on-target) $E_L = (200 \pm 15)$ J was fixed. The focal spot FWHM diameter was 7.3 μm, giving a calculated peak intensity, I_L, equal to 2×10^{20} W cm^{-2} (normalized light amplitude of $a_0 = 13$) for the single pulse case.

A single plasma mirror was used in the focusing beam to enhance the contrast. Figure 1(a) shows an example temporal contrast measurement made of the combined preamplifiers, stretcher and compressor systems using a scanning third order cross-correlator (Sequoia). This detailed scan was made with low power pulses and represents the inherent intensity contrast of the laser pulses, i.e. without plasma mirrors. The contrast enhancement produced by the plasma mirror cannot be measured using the same scanning technique due to the requirement to operate the plasma optics with full power pulses and therefore in single-shot mode. Instead the effect of the plasma mirror is modelled using experimental characterization measurements of the plasma mirror reflectivity as a function of peak intensity [16]. From this the enhancement in the intensity contrast on the rising edge of the laser pulse is determined and is also shown in figure 1(a). The corresponding plot in the picosecond region of the laser pulse rising edge is shown in figure 1(b) on a linear axis. To quantify changes to the intensity on the rising edge we introduce parameter I_{RE} as the intensity at an example time of 1.5 ps prior to the peak of the pulse. We note that even with a plasma mirror the minimum value of I_{RE} is $\sim$0.04 I_L, and this therefore corresponds to the single pulse case in the experiment. The addition of the variable intensity prepulse increases I_{RE} up to a maximum value of $0.2 I_L$. Example on-shot autocorrelation measurements in the single and double pulse modes are also shown in figure 1(b), together with a reference Gaussian pulse.

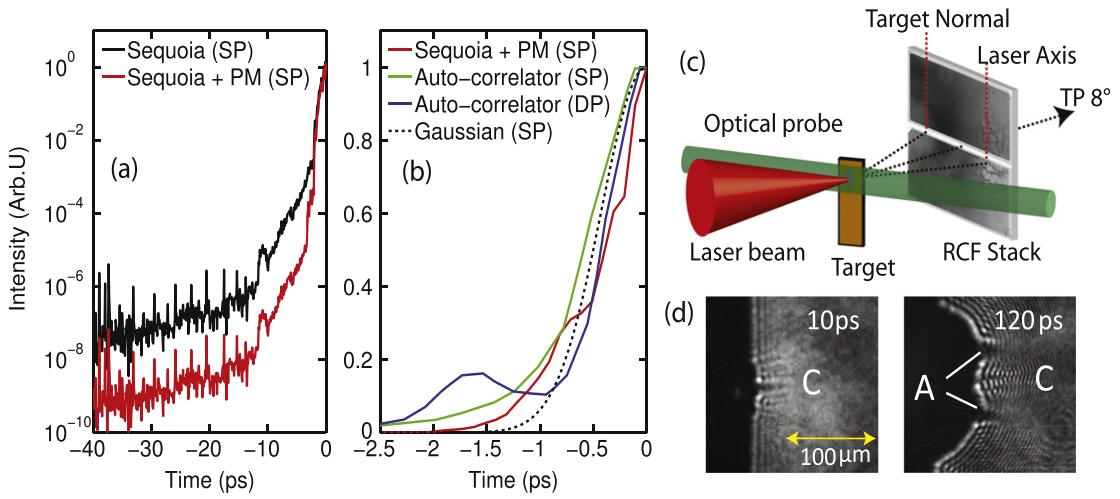

Figure 1. (a) Third-order autocorrelation measurement of the rising edge profile of the laser pulse—black; modelled contrast enhancement due to the plasma mirror—red. (b) Same plot as the modelled contrast enhancement in (a), but on a linear intensity axis and scaled to view the picosecond rising edge of the pulse (red). Example autocorrelation measurements of a single (SP; green) and double-pulse (DP; blue), illustrating the controlled enhancement of I_{RE}. The dotted curve corresponds to a reference Gaussian pulse with FWHM of 1 ps. (c) Schematic illustrating the experimental arrangement. (d) Example optical probe images of rear-surface plasma expansion for a $L = 40$ nm target after 10 ps and 120 ps. Features consistent with channel formation and ring-like expansion are labelled C and A, respectively. The spatial scale is the same for both images.

The angle of incidence, θ_L, was either near-normal or 30° with respect to target normal. The oblique incidence angle was chosen to be sufficiently large to clearly separate the proton beam components directed along target normal (i.e. TNSA) and along the laser axis (i.e. RPA in expanded plasma), while ensuring complete collection of all components on the detector. Figure 1(c) shows a schematic of the arrangement. The laser was linearly-polarized (p-polarization for $\theta_L = 30°$). The target foils were Al with thickness, L, equal to 10 nm or 40 nm, chosen because RIT occurs in both and to differing extents. The laser energy transmitted through the targets was sampled and found to be typically a factor of 2.5 higher for 10 nm compared to 40 nm Al. There was no transmission detected on test shots with 100 nm Al. Protons and carbon ions are produced from hydro-carbon contamination layers on the target surfaces.

The spatial-intensity distribution of the beam of accelerated protons was measured in coarse energy steps using a stack of dosimetry (radiochromic, RCF) film, positioned 7.5 cm from the target. The dimensions of the RCF were 6.4 cm × 5.0 cm. A slot provided a line-of-sight to a Thomson parabola ion spectrometer [17] with calibrated Image-Plate detector [18]. This was used to measure the charge-to-mass ratio (q/m) and energy spectrum of ions accelerated along a sample angle of 8° from the laser axis. The diagnostic low energy detection threshold for protons was 5 MeV and the spectral measurements were background-subtracted. A transverse optical probe was used to monitor the plasma expansion profile at the target rear side. Example probe images are presented in figure 1(d) and show features in the plasma expansion which are consistent with the proton beam measurements and simulations, as discussed below.

Representative measurements of the spatial-intensity distribution of the protons are shown in figure 2 for $\theta_L = 0°$ and 30°, for $I_{RE} = 0.04I_L$ (i.e. single pulse) and $I_{RE} = 0.1$–$0.2I_L$ irradiation, and for $L = 10$ and 40 nm. The red cross and circles mark the laser axis and the 15° and 30°radii, respectively. Three main features are observed: feature A is a ring-like distribution centred along the target normal direction; B is a bubble-like distribution centred along the laser axis; and C is a narrow divergence, high energy component which is directed at an angle between the laser and target normal axes. These features are described in more detail below and corresponding signatures in the experiment and simulation results are hereinafter labelled A, B and C accordingly. We note that the spatio-temporal distribution of the laser focal spot [19] and pulse front tilt [20] can both affect the spatial-intensity distribution of the beam of accelerated protons. However, neither of these parameters are varied in the present study and do not account for the observed features.

The [$\theta_L = 0°$; $I_{RE} = 0.04I_L$; $L = 10$ nm] example measurement shown in figure 2(a) is dominated by feature A —an annular (ring) profile with divergence half-angle of ~12°. A similar feature has been observed with diamond-like carbon foils undergoing RIT [11, 21]. It is attributed to the buffering effect of heavy ions producing a radial force as they push into the proton layer—the heavy ions having gained additional energy from an enhancement in the electrostatic field due to the volumetric heating of target electrons when RIT occurs [21]. The effect is described in more detail with reference to simulation results in the next section. As shown in figure 2(b), for [$\theta_L = 0°$; $I_{RE} = 0.1I_L$; $L = 10$ nm], when increasing I_{RE} bubble-like structures (feature B), which

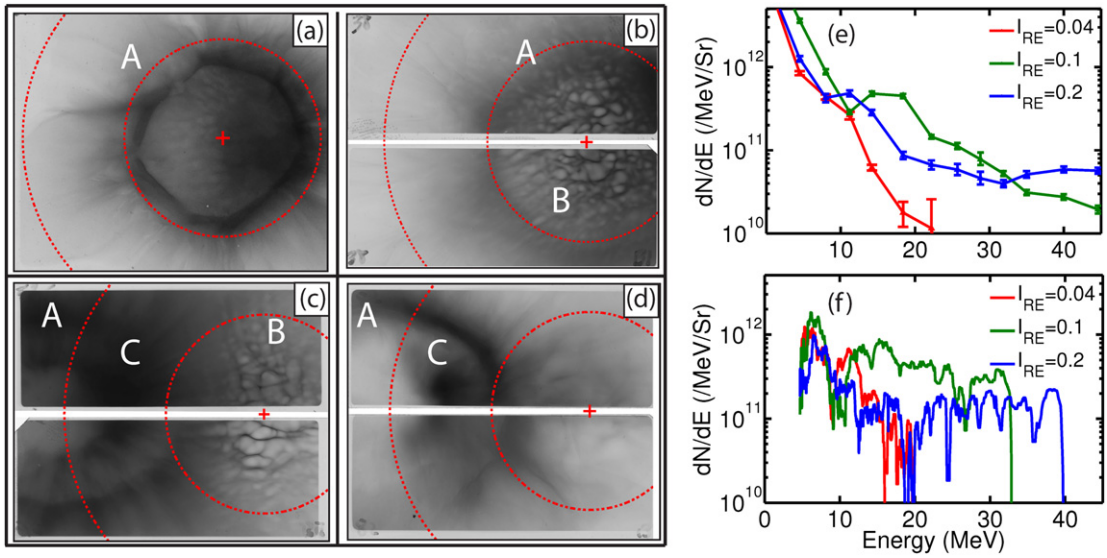

Figure 2. Proton spatial-intensity profiles in the energy range 5–7 MeV, for: (a) [$\theta_L = 0°$; $I_{RE} = 0.04 I_L$; $L = 10$ nm]; (b) [$\theta_L = 0°$; $I_{RE} = 0.1 I_L$; $L = 10$ nm]; (c) [$\theta_L = 30°$; $I_{RE} = 0.1 I_L$; $L = 10$ nm]; (d) [$\theta_L = 30°$; $I_{RE} = 0.2 I_L$; $L = 40$ nm]. The red cross marks the laser propagation axis and the circles mark the radii at 15° and 30°. The features labelled A, B and C are discussed in the main text. (e) Proton energy spectra in the region of feature C, as measured using the RCF stack, for three example I_{RE} (all for $\theta_L = 30°$ and $L = 40$ nm). (f) Corresponding proton energy spectra as measured using the Thomson parabola spectrometer at 8° to the laser axis.

have been shown to arise from Rayleigh–Taylor-like transverse instabilities in RPA [6], are clearly observed within the ring. Figure 2(c) shows the effect of tilting the target by 30° ([$\theta_L = 30°$; $I_{RE} = 0.1\ I_L$; $L = 10$ nm]). The bubbles are formed in the proton population centred along the laser propagation direction (which is consistent with RPA in targets undergoing expansion), whereas the ring is centred along the target normal axis in all shots. Feature C, the enhanced region of proton density and maximum energy, is observed near the edge of the ring, at an angle of ~15°–25° from the laser axis. This feature is more clearly observed for $L = 40$ nm targets, as shown in figure 2(d) ([$\theta_L = 30°$; $I_{RE} = 0.2 I_L$; $L = 40$ nm]). Feature C moves around from shot-to-shot within a ~10° angular range. On many shots it overlaps with a localized region of the ring, giving rise to an arc-shaped population of higher energy protons on the RCF, and in other shots, where it does not overlap the ring, it is approximately circular, as shown in figure 2(d). The origins of this feature and the reasons for its movement are discussed in the next section with reference to simulation results.

Due to the movement of feature C it was not possible to measure the corresponding proton spectrum with a fixed spectrometer sampling a small angular range. Instead, the spectra in the region of this feature was obtained from the RCF stack and is shown in figure 2(e) for given I_{RE}. Corresponding spectra as measured using the spectrometer at 8° are shown in figure 2(f). Both sets of measurements show an extension of the spectrum to higher energies as I_{RE} is increased, highlighting an overall enhancement in ion energies in the angular region between the laser axis and target normal. The largest energy enhancement is measured in the region of feature C.

3. Simulations

We investigate the underpinning physics by performing 2D and 3D particle-in-cell (PIC) simulations using the EPOCH code [22] with parameters chosen to be comparable with the experiment. As shown below, the main features of the interaction are observed in both sets of simulation results. The computationally intensive 3D simulations were performed to ensure that the same behaviour is observed in the higher dimension, to obtain another estimate of the expected ion energies (which is known to be sensitive to the dimensionality of the simulation) and to discount the impact of any potential asymmetric effects driven by the linear polarization (for example those explored in [10, 23]).

The simulation box for the 2D runs was 175 μm × 65 μm, using 26000 × 3840 mesh cells and 50 particles per cell. The target was angled at 30° to the laser axis (to match the experiment) and was initialised as a 40 nm thick layer of $60 n_c$ Al^{11+} (the density of solid aluminium), with 8 nm thick hydrocarbon contamination layers composed of $60 n_c$ H^+ and $20 n_c$ C^{6+} on both surfaces. The thickness and relative densities of the contamination layers is consistent with those expected experimentally and used in previous numerical investigations (e.g. [24]). Test simulations with the EPOCH PIC code incorporating an ionization model showed that for the parameter range explored in this investigation the predominant ionization state reached in aluminium and carbon is

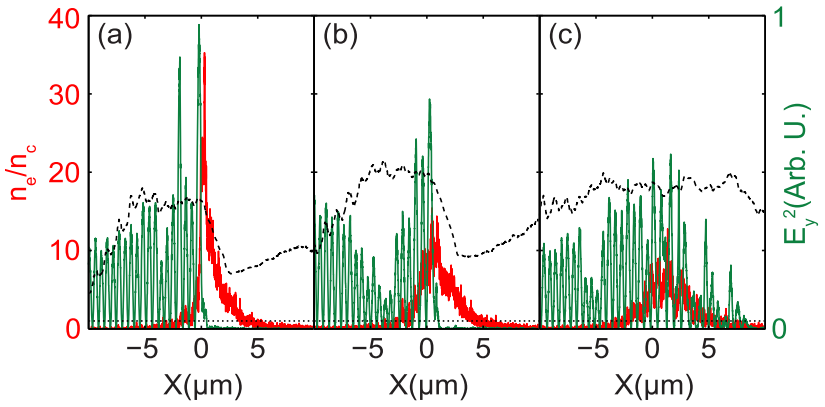

Figure 3. Line-outs along the laser propagation axis for the target electron density in red, the critical density (n_c) in the dotted black line, the relativistically corrected critical density (γn_c) in dashed black (all left axis) and the laser E-field squared in green (right axis). These plots corresponds to: (a) 560 fs, (b) 600 fs and (c) 640 fs into the simulation and the peak of the laser pulse reaches the target at 700 fs. The example 2D simulation is the same one shown in the top row in figure 4 (the $I_{RE} = 0$ case). In (a) the target is still overdense (i.e. $n_e > \gamma n_c$), in (b) the target has just reached the condition of full RIT (i.e. $n_e < \gamma n_c$) and in (c) a portion of the laser pulse has propagated through the target.

q=11+ and 6+, respectively, and so these ion species are used for all of the simulation runs discussed in the paper. The initial electron temperature was set to 10 keV, chosen to be low enough to minimize pre-expansion of the target prior to the arrival of the laser pulse, but high enough to resolve the Debye length as closely as possible. The laser pulse had a Gaussian temporal envelope with a FWHM of 0.5 ps and was focused to a Gaussian intensity profile with FWHM of 6 μm. The peak intensity was 2×10^{20} W cm^{-2} (to match the experiment). The rising edge profile was varied by using a prepulse of the same duration, with peak-to-peak separation of 1 ps. I_{RE} was varied up to $0.5I_L$, reducing the peak intensity to keep the energy fixed (as in the experiment).

Due to computational constraints, the numerically intensive 3D runs used a 60 μm $\times$ 20 μm $\times$ 20 μm simulation box with 3000 $\times$ 360 $\times$ 360 cells and 20 particles per cell. To compensate for the reduction in resolution and box size, the target consisted of the equivalent of 20 nm Al^{11+} at a density of $60n_c$, expanded to a Gaussian profile with a peak density of $5n_c$ (informed by the 2D results). Similarly the H^+ and C^{6+} layers were expanded to a peak density of $5n_c$ and $1.67n_c$, respectively. The initial electron temperature was again 10 keV. The two laser pulses were again focused to 6 μm, but the pulse durations were reduced to 0.2 ps (FWHM) with a 0.5 ps separation, to make the 3D simulations feasible. Test simulations with pulse durations from 0.2 to 0.8 ps showed similar behaviour in all cases for which RIT occurs.

The simulation results demonstrate that the target undergoes RIT on the rising edge of the laser pulse. This is shown in figure 3, for which n_e and γn_c are plotted, together with the laser intensity, along the laser propagation axis at three example times (560 fs, 600 fs and 640 fs after the start of the simulation) on the pulse rising edge (the peak of the laser pulse reaches the target at 700 fs). In figure 3(a) $n_e > \gamma n_c$ and the target is therefore still overdense. In figure 3(b), 40 fs later, n_e has decreased just below γn_c, corresponding to the onset of transparency and in figure 3(c), another 40 fs later, $n_e < \gamma n_c$ and part of the laser pulse is transmitted.

Example results at a later time in the 2D and 3D simulations (after transparency has occurred) are shown in figures 4 and 5, respectively. The overall picture emerging from the simulations is as follows. Electrons accelerated by the laser at the target front side early in the interaction drive sheath acceleration on both sides of the target. The proton population expands faster than the lower q/m Al and C ions, resulting in layering of the ion species (see for example figure 4(c)). As the laser intensity continues to rise, the expanding critical density surface deforms due to the increasing radiation pressure (as discussed for example in [25]). When the condition $n_e < \gamma n_c$ is reached the transmission of the remainder of the laser pulse drives additional electron heating over the target volume. The heated electrons extend over a radius of tens of microns at the target rear, as shown in figures 4(b) and (f), because the radial ponderomotive force due to the propagating part of the laser pulse drives the electrons radially outwards. This behaviour is clearly observed in the 3D simulations and is consistent with [10, 23]. As discussed in the context of BOA [10, 11], in addition to a general enhancement in the acceleration electric field, energy exchange between these electrons and the background sheath-accelerated ions can occur via a relativistic Bunemann instability [12].

In agreement with the experimental results, the simulations exhibit a ring-like proton distribution centred along the target normal, labelled A in figures 4(c) and (g). This feature is not directly induced by the additional heating or radial expansion of the electron population (which is centred along the laser axis), but is produced by the acceleration of heavier (C and Al) ions into the expanding TNSA proton population [21]. An electrostatic

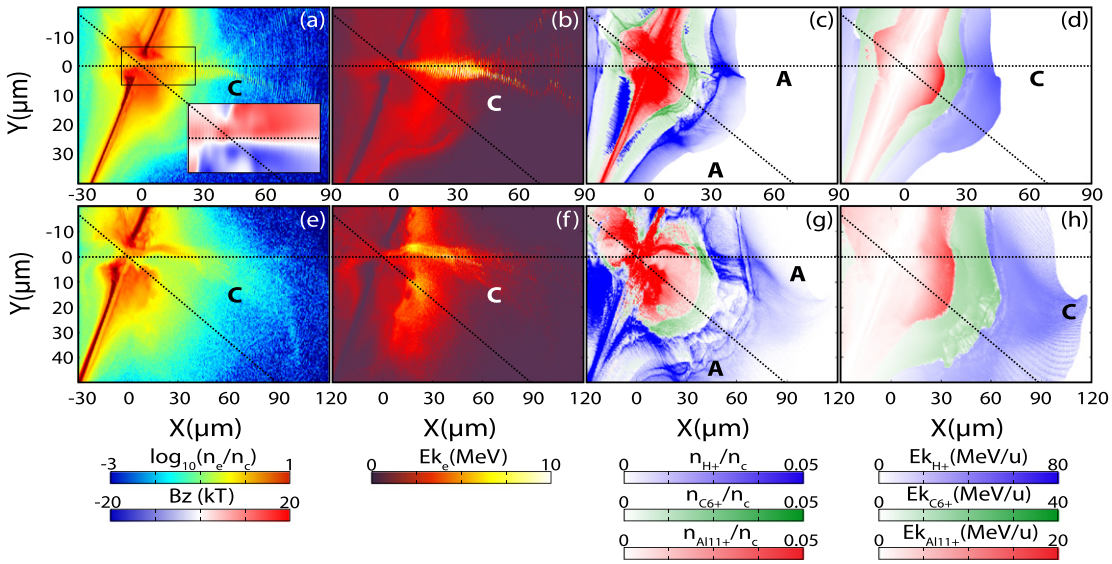

Figure 4. Top row: 2D PIC results showing (a) electron density and magnetic field (inset), (b) mean electron energy, (c) ion density (protons—blue; C^{6+}—green; Al^{11+}—red) and (d) mean ion energy, all for $I_{RE} = 0$ at an example time of 1 ps (300 fs after the peak of the laser pulse reaches the target; 400 fs after transparency is induced). The laser pulse is incident from the left along the $Y = 0$ axis. The dotted lines mark the laser and target normal axes. Bottom row: same for $I_{RE} = 0.2I_L$ at the same time relative to the peak of the main pulse.

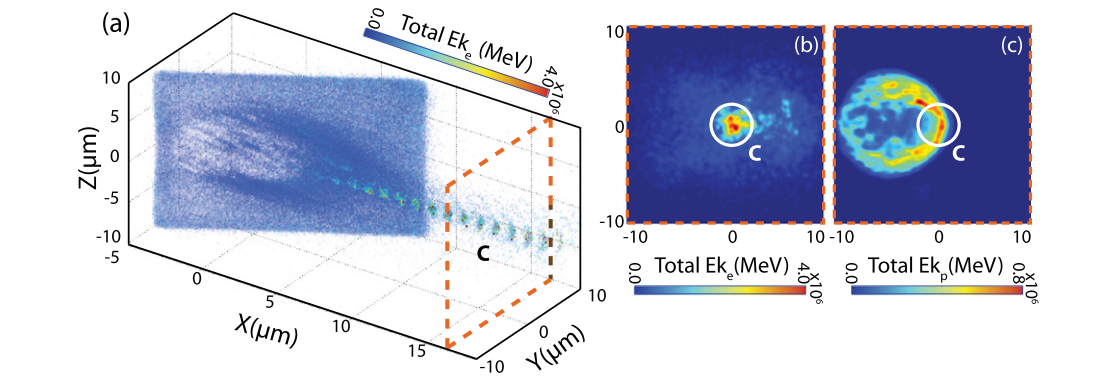

Figure 5. 3D PIC results showing (a) an example 3D plot of the total electron energy at 0.4 ps for $I_{RE} = 0$, and 2D maps of the total (b) electron and (c) proton energies in the Y–Z plane at $X = 16$ μm. At this relatively small distance from the target the channel (labelled C) is on-axis and overlaps with one side of the expanding proton ring distribution. At larger distances it steers off-axis as shown in figure 4(f).

field exists at the interface of different ion species. Following RIT, as the heavy ion population is accelerated forward into the low energy part of the proton distribution, off-axis protons gain momentum in the radial direction. Integrated over time the low energy part of the proton distribution evolves into a ring profile downstream. We note that the transverse optical probe measurements in figure 1(d) show a region of enhanced density either side of target normal (again labelled A), which is consistent with ring-like expansion.

The most salient new feature of our simulation results is the observation that the onset of RIT is accompanied by the formation of a jet of superthermal electrons extending into the expanded ion layers — feature C in figures 4 and 5. The jet is bounded by a magnetic field, which is shown in the inset of figure 4(a) for the region around the target highlighted by the rectangular box. Jet-like current streams of this type can be produced in magnetized channels or magnetic vortex-driven current structures generated when fast electrons are turned around in the sheath field formed at the rear of a plasma slab [13]. We note that a plasma channel or jet-like feature extending from the rear of the target is observed experimentally in the transverse optical probe measurements in figure 1(d) at early times after the interaction (at 10 ps).

Due to the co-propagation of the transmitted part of the laser pulse with the jet, direct acceleration of electrons occurs over an extended distance, resulting in electron energies significantly higher than the

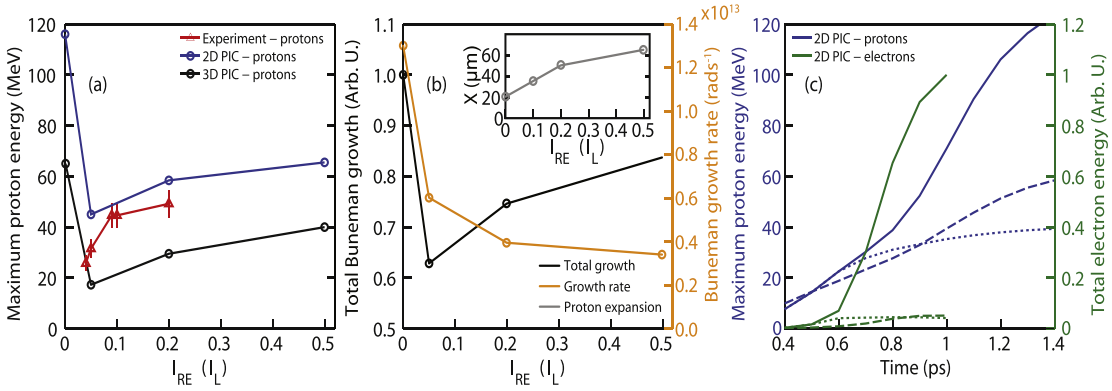

Figure 6. (a) Maximum proton energy in the experiment (red), and 2D (blue) and 3D (black) simulations as a function of I_{RE}. (b) The scaling of the calculated relativistic Buneman instability growth rate (orange) and total growth (black) as a function of I_{RE}. The inset is a plot of the scaling of the width of the proton layer, as extracted from the simulations and used in the growth calculations. The overall trend in the relativistic Buneman instability growth is in good qualitative agreement with the maximum proton energy scaling. (c) Temporal evolution of the maximum proton energy (blue) and total electron energy (green) behind the target, for $I_{RE} = 0$ and three cases: (1) solid—$L = 40$ nm with RIT; (2) dotted—$L = 40$ nm with the laser pulse truncated immediately prior to RIT; (3) dashed—$L = 800$ nm with the full laser pulse (no RIT). The electron traces are truncated at 1 ps when the electrons reach the end of the simulation grid.

surrounding plasma. This is observed in both the 2D and 3D simulations (e.g. in figures 4(b) and 5(a), respectively). Note that the electrons within the jet are bunched as a result, as clearly observed in figure 5(a).

The additional electron energy is in turn coupled to protons in the vicinity of the jet. We note that although a magnetized channel may account for the production of the electron jet, the parameters of the present study are unsuitable for accelerating ions via the magnetic vortex acceleration scheme [14]. That scheme requires a well-defined localized magnetic field structure, such as produced at a plasma boundary, which moves in a non-uniform plasma producing a localized moving longitudinal electric field structure. In the present study, the expansion characteristics of the target produce non-localized magnetic and electric field structures. The mechanism of energy coupling between the electrons in the jet and the background ions is addressed in the next section.

Initially directed along the laser axis, after tens of microns the plasma jet steers by 10°–15° due to the local asymmetry in the background plasma density arising from the target tilt. This results in the highest energy protons being produced in a narrow angle, off-axis region, amongst a broader angular distribution of lower energy ions, as shown in figures 4(d) and (h) and in figure 5(c). This is fully consistent with the experiment results for which the highest energy protons are measured in the RCF at or near the edge of the proton ring (feature C in figures 2(c) and (d)). Thus we find that several key features of our experiment results are accounted for in the simulations.

4. Energy exchange and sensitivity to the laser rising edge profile

In this section we consider the scaling of the maximum proton energy of feature C with I_{RE} and the mechanism underpinning the energy enhancement. The experiment and 2D and 3D PIC simulation results are compared in figure 6(a). We note that the case $I_{RE} = 0$, corresponding to an idealized ultrahigh contrast laser pulse, produces the highest proton energy in the simulations. The maximum energy is significantly lower for the non-idealized contrast cases accessible experimentally. For $I_{RE} \geqslant 0.04$ the energy increases with I_{RE} in both the experiment and simulations. Compared to experiment, the predicted energies are higher in the 2D and lower in the 3D case, but these absolute values depend on the laser pulse duration and simulation times (which are shorter for the more computationally intensive 3D runs).

Increasing the intensity on the pulse rising edge increases the degree of plasma expansion, and therefore increases the width and decreases the density of the expanded proton layer. It also affects the distance over which the plasma jet extends. It is at the limit of the expanded plasma that the current propagation cannot be sustained due to the lack of background free electrons to provide a return current. The jet becomes susceptible to hosing-like instabilities beyond this. Magnetic fields generated by the flow of energetic charged particles in background plasma scale with the particle and plasma densities (see for example [26] for a recent characterization of magnetic fields of this type).

In the case of the ultrahigh contrast laser pulse ($I_{RE} = 0$) very little expansion occurs prior to RIT and therefore the layer of protons is close to the region of jet formation. In this scenario, the jet extends over the full

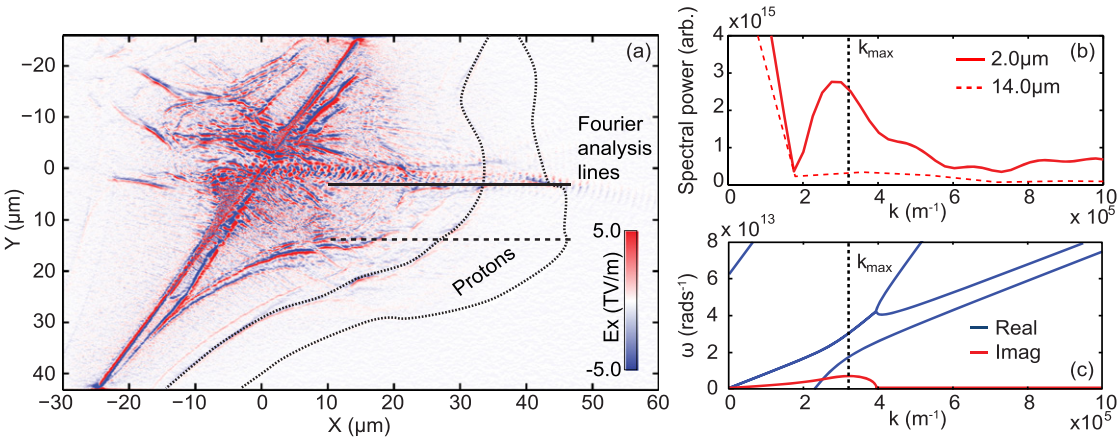

Figure 7. (a) 2D PIC results showing the longitudinal electric field for $I_{RE} = 0$ at an example time of 1 ps (i.e. 300 fs after the peak of the laser pulse reaches the target; 400 fs after transparency is induced). The dotted regions mark the extent of the front and rear of the proton layer and the field driven by the jet is observed to extend into it. (b) Spectral power as a function of wavenumber k along the solid ($Y = 2$ μm) line in (a), which marks the region along the jet at which the highest energy protons are produced, and dashed ($Y = 14$ μm) line, a region spatially off-set from the jet.(c) Analytic solutions to the linear dispersion relation for the Buneman instability, as discussed in the main text. The maximum wave growth occurs at k_{max}, which is in very good agreement with the wavenumber of the longitudinal E-field driven by the plasma jet ($Y = 2$ μm in (b)).

dense proton layer, as shown in figures 4(a)–(d) (where the proton front reaches $X = 60$ μm and the jet extends to this point before becoming unstable). Additional energy coupling to the highest energy, sheath-accelerated protons can occur in this case. This prediction could not be tested experimentally in this study due to the contrast limitation of the laser pulses. Even a relatively small I_{RE} value of 0.04 produces significant proton layer expansion prior to RIT and thus less favourable conditions for the electron jet to couple energy into the protons. However, as observed both experimentally and numerically, as I_{RE} is increased further the proton energy increases.

To explain this observation we next consider the mechanism of energy transfer between the fast electrons in the jet and the sheath-accelerated protons, and the sensitivity of this to the pulse rising edge intensity profile. In the BOA scheme the streaming between the target electrons volumetrically heated during RIT and the background ions is invoked to explain measured enhancements in ion energy [12]. This occurs via the growth of the relativistic Buneman instability. We consider whether this instability plays a role in energy coupling to protons when the energetic electrons in the plasma jet propagate into the sheath-accelerated proton layer. Although the mass difference between the electrons and the protons may at first appear to make this an unlikely candidate to induce efficient energy transfer, it should be noted that relativistic increases in the mass of electrons in the jet on the order of ~20–60 (~10–30 MeV electrons) reduces the electron plasma frequency considerably.

To explore the potential role of the relativistic Buneman instability, we have performed a Fourier analysis along the longitudinal electric field in the region of maximum proton energy enhancement at the vicinity of the electron jet ($Y = 2$ μm) as well as in a region away from the electron jet ($Y = 14$ μm). Figure 7 shows a plot of the longitudinal component of the electric fields induced by the particles (i.e. with the laser field removed) for the simulation reported in figures 4(a)–(d). A strong longitudinal electric field is produced along the plasma jet and extends into the proton layer, overlapping with the highest energy protons (see figure 4(d)). The spatial structures present along the lines in figure 7(a) are investigated. The $Y = 2$ μm line in figure 7(b) shows a strong spatial structure in the region of wavenumber, k, between 2×10^5 and 4×10^5 m^{-1} which grows over time. By contrast, at $Y = 14$ μm there is no evidence of any similar field structures. For the sake of clarity of the figure we present the analysis at a single point in time and compare with that expected from the growth of the relativistic Buneman instability. The analysis at different times in the simulation is available as a supplementary figure.

Using mean proton and electron plasma frequencies, ω_p, and velocities, v, along the $Y = 2$ μm analysis line, the following linear equation for the relativistic Buneman instability is solved:

$$\frac{\omega_{pi}^2}{\left(\omega - kv_i\right)^2} + \frac{\omega_{pe}^2}{\left(\omega - kv_e\right)^2} = 1. \quad (1)$$

The relativistic factor is incorporated into the determined electron plasma frequency. This results in the dispersion relation shown in figure 7(c). The real solutions correspond to waves that can propagate due to the coupling of the plasma oscillations of the different particle populations. The instability can grow in the region where there are complex solutions to the dispersion equation. It can be seen that the maximum wave growth

occurs at $k_{max} \approx 3.2 \times 10^5\ m^{-1}$ (given by the imaginary component of the complex solution). We note that the wavenumber of this instability is significantly smaller than the wavenumber of the electron jet modulations ($k \approx 6 \times 10^6\ m^{-1}$) and is therefore not directly correlated with the laser-driven modulations. These dispersion solutions are indicative of a set of fixed plasma frequencies and velocities, whereas in the simulation these values are evolving in both space and time. Nevertheless, this simple approximation gives good agreement with the spatial structure growing in the simulations. The value of k_{max} is in very good agreement with the wavenumber of the longitudinal E-field driven by the plasma jet, as shown in figure 7(b). This provides an indication that the energy transfer mechanism from the electron jet to the protons may be mediated by the relativistic Buneman instability, but it should be noted that other process may provide a similar wavenumber signature.

The wave from this instability induced by electrons streaming through the proton layer can only grow over the longitudinal extent (width) of the proton layer. Due to the coupling of the velocities of the electrons and the protons, typically the group velocity of the wave is ~0.4c. This gives a finite time for the wave to grow and couple energy from the electrons to the protons. By increasing the intensity of the rising edge of the laser pulse, the proton layer expands further whilst simultaneously reducing the proton density, prior to RIT. The density decrease has the effect of reducing the growth rate of the relativistic Buneman instability, but the increase in the layer width provides a longer interaction length for the wave to grow. The formation of the electron jet provides a localized increase in energy within the proton layer that reduces the spatial wavevector and angular frequency of the wave closer to that of the expanding protons, facilitating increased energy coupling. From the simulation data approximate growth rates and group velocities, as well as the spatial extent of the proton layer, can be determined for the different values of I_{RE}. This enables the total growth of the unstable wave across the extent of the proton layer to be estimated.

The results of this analysis are shown in figure 6(b). The variation in the relativistic Buneman instability growth with I_{RE}, as determined by the width and density of the expanded proton layer, is in good qualitative agreement with the changes to the maximum proton energy. The high growth for $I_{RE} = 0$ is due to the high proton density in the vicinity of the jet. For $I_{RE} = 0.04$ the proton density has dropped considerably with a corresponding reduction in instability growth. As I_{RE} is increased the densities, and thus the growth rates, continue to reduce, albeit at a slower rate. However, as the proton layer expands, the unstable wave can propagate over an increased distance, increasing the total growth for higher I_{RE}. Whilst this simple analysis does not take into account the full dynamic nature of the system, it provides an indication of how the energy exchange process is sensitive to the laser rising edge intensity profile.

This analysis has focused on investigating the potential for the relativistic Buneman instability to couple energy from the electrons to the ions as outlined by Albright *et al* [12]. Due to the complex dynamics involved in the laser–plasma interaction this does not provide a complete understanding of the energy exchange. Other mechanisms may produce similar features seen in the analysis, such as ion acoustic waves driven by an electron–electron two-stream instability [27]. A full analysis of the various energy-exchange mechanisms will therefore be the subject of future work.

Finally, we consider the degree of energy enhancement produced by this process over purely sheath-accelerated protons. Figure 6(c) shows the temporal evolution of the total electron energy from an example simulation result, which rapidly increases when RIT occurs at 0.6 ps. After a slight delay there is a corresponding increase in the proton acceleration (significant change in the slope at 0.8 ps), resulting in an overall maximum energy enhancement of a factor of ~3 over the TNSA-protons set in motion before RIT occurs. The increase is a factor of ~2 over TNSA driven by the full laser energy on a target which does not undergo RIT.

5. Discussion

The results provide new insight into the complex physics occurring in ultrathin foils undergoing relativistic induced transparency. It is shown that TNSA, RPA and transparency-enhanced/BOA acceleration can all occur, at different stages in the laser pulse interaction with the target, and that the individual mechanisms can be investigated by angularly separating the ion beams produced.

An important new feature observed in numerical simulations of the interaction is that for sufficiently expanded plasmas RIT drives the formation of a plasma jet, supported by a self-generated quasi-static azimuthal magnetic field. Electrons trapped within this jet are directly accelerated to super-thermal energies by the co-propagating portion of the laser pulse which is transmitted through the target. The streaming of these energetic electrons into the sheath-accelerated proton layer enhances the energy of the proton population in the vicinity of the jet. The scheme accounts for a high energy proton component measured experimentally over a narrow angular range, directed between the laser and target normal axes. It is further demonstrated that in the absence of an ultrahigh contrast drive laser pulse, controlled target expansion by variation of the rising edge intensity profile on the picosecond timescale produces better energy coupling to the expanded proton population.

On a practical level, the results highlight the importance of diagnosing and controlling the intensity contrast, not only in the tens of picosecond to nanosecond temporal range explored previously [28–30], but also on the picosecond rising edge of the laser pulse. A similar conclusion has recently been reached based on high fidelity modelling of TNSA acceleration in thicker targets [31]. This task is non-trivial and will require significant investment. However, given the demonstrated importance of the pulse picosecond rising edge profile and the fact that ultrathin foil targets are used in a number of the most promising new laser-ion acceleration schemes (in particular RPA and BOA), this step is important to the future development of laser-ion sources.

Acknowledgments

We acknowledge the support of Central Laser Facility staff and the use of the ARCHIE-WeST and ARCHER computers. We also acknowledge fruitful discussion with Dr Bengt Eliasson (University of Strathclyde). This work is supported by EPSRC (grants: EP/J003832/1, EP/L001357/1, EP/K022415/1, EP/J002550/1 and EP/L000237/1), the US Air Force Office of Scientific Research (grant: FA8655-13-1-3008) and LASERLAB-EUROPE (grant: 284464). LCS acknowledges the EU-funded LA^{3}NET consortium (grant: GA-ITN-2011-289191). EPOCH was developed under EPSRC grant EP/G054940/1. Data associated with research published in this paper is accessible at http://dx.doi.org/10.15129/8db05e8a-45f3-48f5-8ade-5fc2c36aece0.

References

[1] See Daido H *et al* 2012 *Rep. Prog. Phys.* **75** 056401
Macchi A *et al* 2013 *Rev. Mod. Phys.* **85** 751 and references therein
[2] Wilks S C *et al* 2001 *Phys. Plasmas* **8** 542
[3] Esirkepov T *et al* 2004 *Phys. Rev. Lett.* **92** 175003
[4] Macchi A *et al* 2010 *New. J. Phys.* **12** 045013
[5] Kar S *et al* 2012 *Phys. Rev. Lett.* **109** 185006
[6] Palmer C A J *et al* 2012 *Phys. Rev. Lett.* **108** 225002
[7] Vshivkov V A *et al* 1998 *Phys. Plasmas* **5** 2727
[8] Palaniappan S *et al* 2012 *Nat. Phys.* **8** 763
[9] Sahai A A *et al* 2013 *Phys. Rev.* E **88** 043105
[10] Yin L *et al* 2006 *Laser Part. Beams* **24** 291
[11] Jung D *et al* 2013 *New. J. Phys.* **15** 123035
[12] Albright B J *et al* 2007 *Phys. Plasmas* **14** 094502
[13] Bulanov S V *et al* 2005 *Plasma Phys. Rep.* **31** 369
[14] Nakamura T *et al* 2010 *Phys. Rev. Lett.* **105** 135002
[15] Wagner F *et al* 2015 *Phys. Plasmas* **22** 063110
[16] Ziener C *et al* 2003 *J. Appl. Phys.* **93** 768
[17] Gwynne D *et al* 2014 *Rev. Sci. Instrum.* **85** 033304
[18] Alejo A *et al* 2014 *Rev. Sci. Instrum.* **85** 093303
[19] Kahaly S *et al* 2014 *App. Phys. Lett.* **104** 054103
[20] Zeil K *et al* 2012 *Nat. Commun.* **3** 874
[21] Dover N P *et al* arxiv:1406.3540
[22] Brady C S and Arber T D 2011 *Plasma Phys. Control. Fusion* **53** 015001
[23] Gray R J *et al* 2014 *New J. Phys.* **16** 093027
[24] Carroll D C *et al* 2010 *New J. Phys.* **12** 045020
[25] Vincenti H *et al* 2014 *Nat. Commun.* **5** 3403
[26] Flacco A *et al* 2015 *Nat. Phys.* **11** 409
[27] Mendonça J T *et al* 2005 *Phys. Rev. Lett.* **94** 245002
[28] Kaluza M *et al* 2004 *Phys. Rev. Lett.* **93** 045003
[29] Gray R J *et al* 2014 *New J. Phys.* **16** 113075
[30] Esirkepov T *et al* 2014 *Nucl. Instrum. Methods* A **745** 150
[31] Schollmeier M *et al* 2015 *Phys. Plasmas* **22** 043116